Journal of Colloid and Interface Science 627 (2022) 978–991

Contents lists available at ScienceDirect

Journal of Colloid and Interface Science

journal homepage: www.elsevier.com/locate/jcis

Waste-based nanoarchitectonics with face masks as valuable starting material for high-performance supercapacitors

Joanna Sreńscek-Nazzal [a], Jarosław Serafin [b,*], Adrianna Kamińska [a], Anna Dymerska [c,*], Ewa Mijowska [c], Beata Michalkiewicz [a]

[a] West Pomeranian University of Technology in Szczecin, Faculty of Chemical Technology and Engineering, Department of Catalytic and Sorbent Materials Engineering, Piastów Ave. 42, 71-065 Szczecin, Poland
[b] Department of Inorganic and Organic Chemistry, University of Barcelona, Martí i Franquès, 1-11, 08028 Barcelona, Spain
[c] Department of Nanomaterials Physicochemistry, Faculty of Chemical Technology and Engineering, West Pomeranian University of Technology, Szczecin, Piastów Ave. 42, 71-065 Szczecin, Poland

GRAPHICAL ABSTRACT

ARTICLE INFO

Article history:
Received 9 May 2022
Revised 8 July 2022
Accepted 17 July 2022
Available online 21 July 2022

Keywords:
Carbon-based electrode material
Supercapacitor electrodes
Supercapacitor
Hazardous disposable face masks waste
COVID-19

ABSTRACT

Surgical face masks waste is a source of microplastics (polymer fibres) and inorganic and organic compounds potentially hazardous for aquatic organisms during degradation in water. The monthly use of face masks in the world is about 129 billion for 7.8 billion people. Therefore, in this contribution the utilization of hazardous surgical face masks waste for fabrication of carbon-based electrode materials via KOH-activation and carbonization was investigated. The micro-mesoporous materials were obtained with specific surface areas in the range of 460 – 969 m^2/g and a total pore volume of 0.311 – 0.635 cm^3/g. The optimal sample showed superior electrochemical performance as an electrode material in supercapacitor in the three-electrode system, attaining 651.1F/g at 0.1 Ag^{-1} and outstanding capacitance retention of 98 % after a test cycle involving 50′000 cycles. It should be emphasized that capacitance retention is one of the most crucial requirements for materials used as the electrodes in the supercapacitor devices. In this strategy, potentially contaminated face masks, common pandemic waste, is recycled into highly valuable carbon material which can serve in practical applications overcoming the global energy crisis. What is more, all microorganisms, including coronaviruses that may be on/in the masks, are completely inactivated during KOH-activation and carbonization.

© 2022 Elsevier Inc. All rights reserved.

1. Introduction

The demands for disposable face masks have increased since the beginning of the pandemic and have led to the subsequent generation of hazardous microplastic wastes. Moreover, surgical face mask wastes contain inorganic and organic compounds potentially

* Corresponding authors.
E-mail addresses: jaroslaw.serafin@qi.ub.es (J. Serafin), da36295@zut.edu.pl (A. Dymerska).

https://doi.org/10.1016/j.jcis.2022.07.098
0021-9797/© 2022 Elsevier Inc. All rights reserved.

hazardous for aquatic organisms during degradation in water [1]. The problem is huge because the monthly use of face masks in the world is about 129 billion for 7.8 billion people [2]. The daily use of protective face masks creates environmental problems. In a natural environment, the degradation and fragmentation processes of face masks took place. The mask is degraded into smaller pieces: smaller than 5 mm - microplastics and smaller than 100 nm – nanoplastics [3] and possesses a potential risk.

So far, standard technologies for the treatment of hazardous waste materials are mainly based on thermal processes such as incineration, steam treatment (autoclaving), plasma treatment and microwave treatment [4]. Considering the available technological options for the treatment of waste from contaminated polypropylene (PP) masks, waste incineration combined with waste heat recovery is an option that allows the recovery of the chemical energy content of plastics for utility purposes. However, the technology of applying heat recovery combustion has some drawbacks related to concerns about releasing harmful toxins into the environment, which adversely affect both the environment and human health [5]. In contrast, autoclaving this type of waste only heats the waste to a temperature sufficient to kill pathogens. As a result, autoclaved waste is often reprocessed by incineration, which makes autoclave processing unnecessary, as it unnecessarily increases disposal costs [6].

Therefore, it is imperative to plan the appropriate disposal of face mask waste by adopting a suitable method that will transform mask waste into useful materials with a higher added value. For example, Yu et al. [7] reported the possibility of catalytic carbonization of bondwaste masks (WMs) into high-value carbon nanomaterials. Received results showed that the resultant products were CNTs / Ni hybrids, and the highest carbon yield was 64.4 g/ 100 g^{-1}WMs. As a result of the synergistic effect of CNTs and Ni, the as-fabricated hybrids exhibited outstanding microwave absorption capacity of strong reflection loss of −56.3 dB and broadband width of 4.3 GHz at the thickness of 2.0 mm.

By contrast, Jung et al [8] obtained valuable fuel by carrying out a thermo-chemical process assisted with CO_2. The authors have used the carbonization from the disposable mask to study the production of syngas and C1-2 hydrocarbons (HCs). To enhance syngas and C1-2 HCs formations, multi-stage carbonization was used for more C—H and C—C bond ions of the disposable mask. Catalytic pyrolysis over Ni/SiO_2 further boosted H_2 and CH_4 formations due to its capability for dehydrogenation. What is more, in the presence of CO_2, catalytic pyrolysis additionally produced CO. Hence, the thermo-chemical conversion of disposable face masks and CO_2 might be an environmentally benign way to remove COVID-19 plastic waste, creating value-added products.

Also, Xu et al. [9] transformed the waste from the masks into useful fuels and chemicals. The authors have developed a carbon foam microwave plasma process, utilizing plasma discharge to generate surface temperatures exceeding∼3000 K in an N_2 atmosphere, to convert face mask wastes into gases like C_2H_4, H_2, CO, CH_4, and C_3H_6.

In addition, there was a report by Liu et al. [10] in which the authors showed a new way to prepare carbon nanosheets from waste polypropylene (PP) using a combined catalyst of sulfur and ferrocene. Currently, processing plastic waste into two-dimensional carbon nanosheets is considered as a promising way to solve these problems due to the high carbon content of plastic waste. Activated Carbon Nanosheets (ACNS), after activation treatment, exhibited a well-defined hierarchical porous structure. In addition, they were characterized by a large specific surface (3200 m^2g^{-1}) and a significant pore volume (3.71 cm^3g^{-1}). In addition, the ACNS-based electrode provides a high specific capacity of 349F/g at 0.5 A/g. The fabricated symmetric supercapacitor manifests a high energy density of 23 W h kg^{-1} at 225 W kg^{-1}.

Aboul-Enein and Awadallah have also used waste plastic polypropylene as a carbon source to synthesize high-quality carbon nanomaterials (CNMs) in a two-step process. Lanthanum oxide (La_2O_3) was used as a promising support of active metals in the thermocatalytic breakdown of hydrocarbons. Monometallic catalysts 50 % Ni and bimetallic 40 % Ni / 10 % Cu on the La_2O_3 support with a total metal content of 50 % by weight were prepared and tested to decompose no condensable gases obtained from the carbonization of PP to produce nanomaterials. A fact worth the examples of research presented above show that promising strategies for the treatment and recycling of plastic waste are being developed, which is especially valuable because plastics have a high carbon content, what is an ideal way to transform this type of waste into important products in the form of carbon materials [11].

The conventional energy sources - fossil fuels such as coal, natural gas, and petroleum are waning as the demand rises [12]. These resources are natural but their formation in a natural environment takes hundreds of thousands of years [13,14]. Therefore, they are considered non-renewable and non-sustainable [15]. Considering these issues, there is a serious need for an effective constant energy supply at a low cost and a way to store it. One of the simple and quick methods is to use electrochemical energy as a power source. The batteries, electrochemical capacitors, and fuel cell devices were found to be promising for the conversion and storage of electrochemical energy [16,17]. Carbon materials with high surface area and pore volume were considered good electrode materials for electric capacitors because of their very good chemical and thermal stability and low cost [18]. The most investigated carbonaceous materials have been graphene, carbon nanofibers, carbon nanotubes, activated carbons, carbon aerogels, nano-sized carbons [19,20]. Recently, fullerene crystals-derived carbon tubes have been also studied as electrode material for high-rate performance supercapacitors [21].

Commonly available carbon precursors can be applied as starting materials for carbonaceous materials production exhibiting high capacitance and good rate capability [9]. Therefore, for this aim, sustainable and commonly available raw materials have been investigated for the fabrication of various carbonaceous materials mainly for supercapacitor applications. Bio – waste such as oil palm leaf [15], palm kernel shells [15], olive bagasse [22], coconut shell [23], hemp straw [24], coconut husk [25], rice husk [26], lumpy bracket [27], lignin [28], kapok flower [29], common polypody [30,31], spent dregs [32], nutshells [33], pomegranate peel [34], pitch [35] have been reported.

Huan Liu and co-workers [36] published lotus leaf stem (biomass) derived O—N—S co-doped carbon for supercapacitor devices with an excellent capacitance of 425F/g at a current density of 0.5 A/g in a 3-el system and 295F/g at a current density of 0.1 A/g with outstanding rate capability with high retention (84 %) while increasing current density from 0.2 to 20 A/g, and outstanding recyclability with 97.8 % retention after 10′000 charge–discharge cycles at 10 A/g in a 2-el system with KOH as an electrolyte. They have also achieved excellent recyclability of 93.3 % after 10,000 cycles at the same current density using Na_2SO_4 solution as an electrolyte. The advantages of their material arise from a 3D hierarchical structure with high surface area and optimized pore size distribution. Moreover, O—N—S co-doping and nanosized graphitic structure lead to a large accessible surface for charge storage, short ion diffusion distance, rapid charge transfer and low internal resistance, which are favourable characteristics for energy storage. Another group – X. Liang et. Al. [37] has also published biomass waste-derived carbon for supercapacitors. The porous carbon obtained by KOH activation foxtail grasses seeds. The as-prepared nitrogen- and sulphur-doped hierarchical porous carbon (NSPC) with an appropriate specific surface area (819 m^2g^{-1}), interconnected porous structure and rich heteroatoms, exhibits

high gravimetric (358.0 Fg^{-1}) and volumetric (243.4 Fcm^{-1}) capacities at 0.5 Ag^{-1} and also impressive cycling stability. Karaman C. et al. [38] reported graphene-like porous carbon networks derived from orange-peel wastes (GPCs) for energy storage. The electrochemical behaviour of GPCs was evaluated in a 6.0 M KOH aqueous electrolyte in a 3-el electrochemical system. The specific capacitance of 425Fg^{-1} was explained due to its synergistic properties, including an excellent specific surface area (1150 m^2g^{-1}, a large pore volume and a finely tuned 3D porous architecture. Another bio-material-based supercapacitor device was made from waste lignin 325F·g^{-1} /1 A·g^{-1} (between − 1 to 0 V) [39], and cellulose 162F·g^{-1} (at 0.5 A·g^{-1} between − 1 and 0 V) [40].

Today, more and more attention is focused on polymeric everyday products, which can be given a second life for applications including energy storage. For example, carbon derived from waste PET bottles, which exhibit a specific capacitance of 413 Fg^{-1} (at 1 A·g^{-1}, in the voltage window from − 1 to 0 V) [41], slightly lower capacitance has shown carbon from expanded polystyrene foam 327F·g^{-1} (1 A·g^{-1}, in the voltage window from − 0.2 to 0.8 V) [42]. Lastly, carbon material made from waste face masks was used as an electrode material for energy storage, which exhibits capacitance of 328.9F·g^{-1} (at 1 A·g^{-1} in the working range between − 0.8 and 0 V) [43]. However, there is still plenty of room for researchers to boost the electrochemical performance of the supercapacitor devices based on biomass/recycled derived products.

Disposable face masks are mainly used in highly contaminated areas, for example, medical centres, public places, and public transportation, which are at high risk of coronavirus contamination. The novelty of the work is to transform the potential dangerous waste into value-added products: carbon electrode materials in supercapacitor with excellent capacitance and retention after 50 000 cycles.

In our study, all the biological hazardous waste will be neutralized because the carbon source is treated with saturated KOH solution and high temperature. The carbon-based electrode materials were obtained by chemical activation followed by carbonization. The temperature of carbonization was changed from 650 to 800 °C every 50°to study the influence of the texture on the electrochemical behaviour of the capacitor. Therefore, this facile strategy serves as a route for the utilization of potentially contaminated face masks - common coronavirus waste.

Furthermore, to the best of our knowledge, the fabricated carbon materials derived from wasted masks have not been tested in current state of the art as electrode material in supercapacitors in their pristine form without any further elemental functionalization. There is a very recent report on carbon-derived samples from wasted masks but the carbonization process was supported by sulfur doping [43]. Additionally, our electrodes indicated boosted electrochemical performance in supercapacitors in respect to state of the art.

2. Materials and methods

2.1. Preparation of carbon-based electrode materials from a disposable mask

Disposable surgical face masks were manufactured by AP PROPERTY S.A. (Poland). The disposable masks were impregnated with a saturated KOH solution in a mass ratio of disposable masks: KOH 1: 1 for 3 h at room temperature. After impregnation, the material was dried in a laboratory drier for 19 h at a temperature of 150 °C. After drying, the grounded material was carbonized in a tube furnace. The temperature range was from 650 to 800 °C with a step of 50 °C under nitrogen flow of 18 L/h. Next, the carbonized product was washed with distilled water to remove the residual KOH until neutral pH. Then the samples were flooded with1 M hydrochloric acid and washed again until neutral pH. Finally, the obtained carbon-based electrode material was dried at 200 °C for 19 h. The names of the samples correspond to the carbonization temperature.

Fig. 1 shows a schematic synthesis of activated carbons.

2.2. Electrochemical capacitor assembly

All obtained material was measured in two- and as well as in three-electrode system for detailed investigation of mechanism and reaction during energy storage.

2.2.1. Preparation of material for electrodes

Electrode material for a two- (2-el), as well as three-electrode system (3-el) was prepared by mixing 100.0 mg of active material, 20.0 mgof acetylene black (20 wt%) and 10.0 mg Kynar Flex poly (vinylidene fluoride) (PVDF) (10 wt%). These components have been mixed with acetone and homogenized with use of Benchmark D1000 Homogenizer for at least 60 s. After that, the mixture was transferred to a glassy crystallizer and dried forming a powder.

2.2.2. Construction of the two electrode system

The working electrodes (WE) for the 2-el were fabricated with 9.1 mg of electrode material (described in section 2.2.1) for each electrode. Next, the materials were pressed to form tablets with diameter of 15.0 mm via Mechanical Tablet Press Machine. Next, the electrodes were dried for 24 h in a vacuum oven (15 mbar, 100 °C). The dried working electrodes (WE) were weighted and assembled in a type CR2032 button cell, with a double layer of separators (cellulose and glass separator) and 6 M KOH as an electrolyte. It was pressed via Oil Hydraulic Press Machine (∼100 MPa) to seal the cell.

2.2.3. Construction of the three electrode system

The WE for the 3-el was produced by pressing ∼ 3.0 mg of electrode material with a few drops of anhydrous acetone at the surface of a circle-shaped nickel foam with diameter of 15 mm. Next, the electrode was dried for 24 h in a vacuum oven (15 mbar, 100 °C). The system was also composed by Mercury Oxide Standard Electrode (MOSE: Hg|HgO, with 1 M KOH as an electrolyte) as the reference electrode (RE) and Stainless Steel Mesh as the counter electrode (CE). 6 M KOH served as the electrolyte.

2.3. Textural characterization of carbon-based electrode materials

The textural characterization of the samples was performed using N_2 adsorption at −196 °C in a volumetric QUADRASORB evo™ apparatus. In order to remove impurities, before the adsorption measurements, the samples were outgassed at the temperature of 250 °C for 12 h with a temperature increase of 10 °C /min at the constant operation of the pump under reduced pressure. For this purpose, a MasterPrep apparatus coupled with a computer was used. The parameters characterizing the porous structure were determined from the N_2 sorption isotherms:

a) the specific surface area (S_{BET}) was calculated from the BET equation in the partial pressure range p/p_0 = 0.05 – 0.2
b) the total pore volume (V_{tot}) was determined on the basis of the maximum adsorption of nitrogen at p/p_0 value = 0.99
c) the micropore volume (V_{mic}), was established using the DFT (density functional theory) method: N_2 at −196 °C on carbon for slit/cylinder/sphere pores, quenched solid density functional theory (QSDFT) adsorption branch method

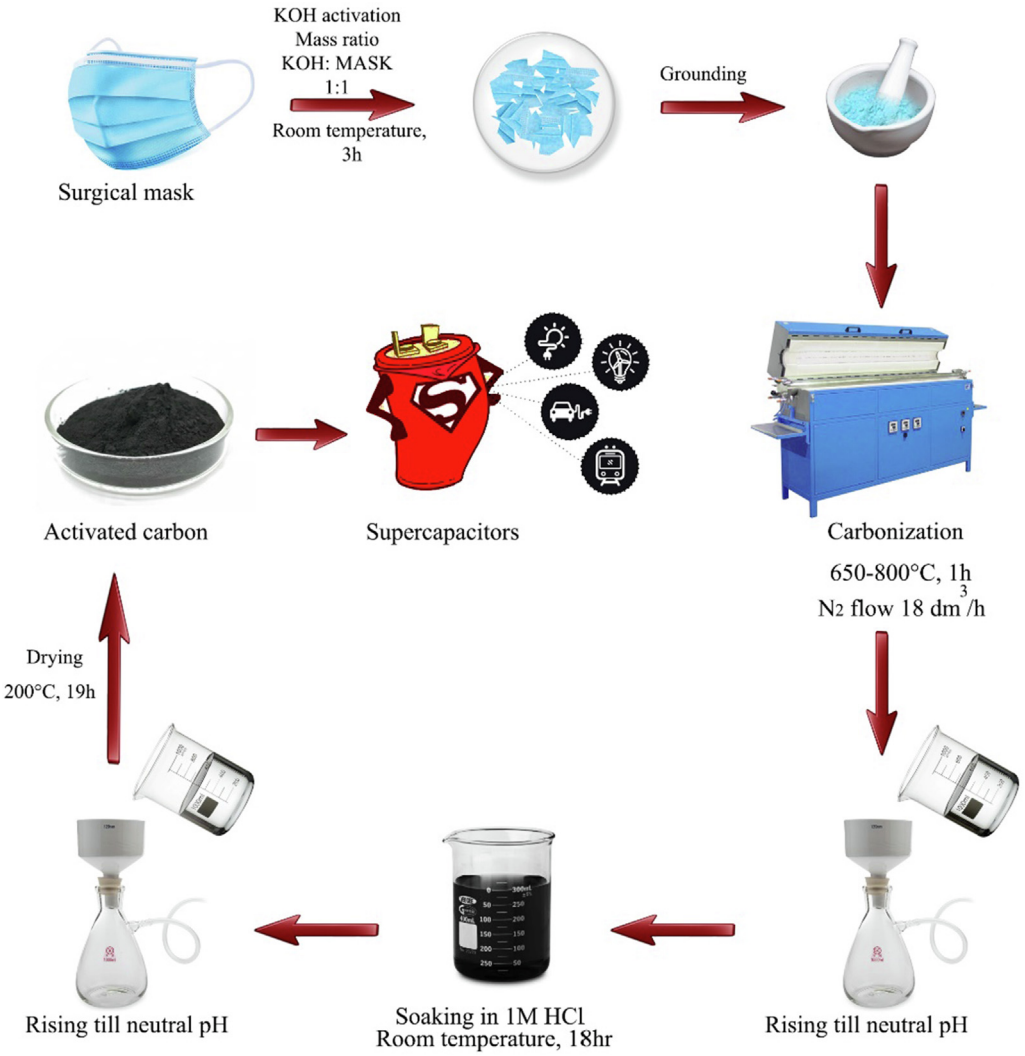

Fig. 1. Schematic visualization of synthesis route of the activated carbons.

The Thermo-Gravimetric Analysis (TGA) was performed using a TA Instruments SDT Q600 under the air atmosphere with a heating ramp of 10 °C min^{-1} in the range between room temperature and 700 °C min^{-1}.

For the determination of the structure of the carbon framework of prepared carbon materials, Raman spectroscopy was used. The analyses were performed using an apparatus Renishaw InVia. A laser induced the material samples with a wavelength of 785 nm.

Surface morphology images of all prepared materials were characterized by SEM instrument Zeiss Neon40 Crossbeam Station instrument at 5.0 kV equipped with a field emission source. The sample preparation for scanning electron microscopy (SEM) involved sprinkling the powder sample on a double-sided carbon tape mounted on the SEM stub.

2.4. Electrochemical tests

EC-Lab VMP3 (*BioLogic Science Instruments, France*) was used to characterise the electrochemical properties of all samples. For this purpose, following electrochemical techniques were performed: Cyclic Voltammetry (CV) at scan rates of 2, 5, 10, 20, 50, and 100 $mV{\cdot}s^{-1}$, Galvanostatic Cycling with Potential Limitation (GCPL) at current densities of 0.1, 0.6, 1.0, 6.5, and 13.0 $A{\cdot}g^{-1}$, and Potentiostatic Electrochemical Impedance Spectroscopy (PEIS) at the frequency range between 10 mHz and 200 kHz, with an alternating current amplitude (AC signal) of 10 mV. Furthermore, the stability test was performed as the charge–discharge test under the constant current density of 2 $A{\cdot}g^{-1}$ for 50′000 cycles. All electrochemical measurements were performed at room temperature in 6 M KOH as an electrolyte in the potential window between 0.0 and + 0.8 V.

3. Results and discussion

3.1. Characterization of disposable mask and carbon-based electrode materials by XRD method

The X-ray diffraction (XRD) patterns of the *disposable mask and carbon-based electrode materials* were investigated with an X-ray diffractometer (X'Pert–PRO, Panalytical,) monochromatic Cu Kα radiation (λ = 0.154 nm).

The crystal structure of the face masks was investigated by XRD method (Fig. 2). The sharp reflections a (111), (131) 2θ = 14.1°, 16.9°, 18.6°, 21.2°, 22.0° corresponding to the (110), (040), (130) diffraction planes were assigned to the α-monoclinic phase of polypropylene [44,45] confirming the presence the crystal structure. The two broad bands cantered around 2θ = 25.5° and 28.5° associated with diffraction of the (060) and (220) planes also

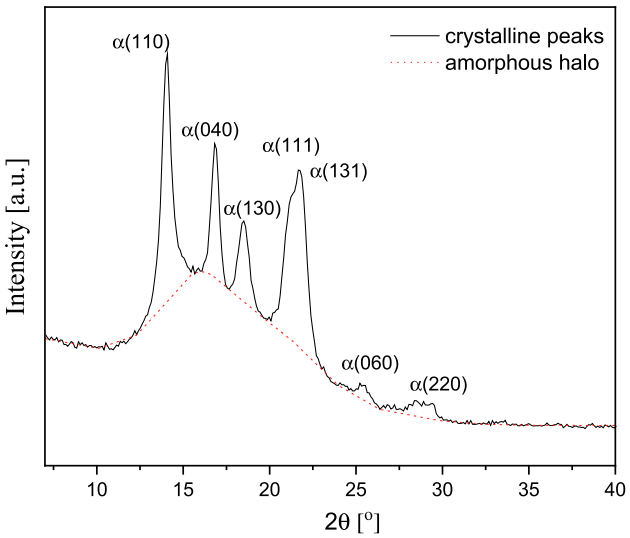

Fig. 2. XRD pattern of the disposable mask.

confirmed the presence of α-monoclinic phase [45]. The broad peaks revealed presence also amorphous carbon structure. A very good visible amorphous halo also confirmed partial amorphousness of the polypropylene present in disposable face mask.

Fig. S1 presents XRD pattern of carbon-based electrode materials revealed only two broad peaks centred at around 2θ = 23° and 43°, corresponding to the the (002) and (10) planes. The broad peaks indicated amorphous carbon structure. After carbonization the polypropylene structure was completely damaged and activated carbon was obtained.

3.2. Textural characterization of carbon-based electrode materials from a disposable mask

The SEM micrographs of carbons derived from disposable face masks are shown in Fig. S2. SEM images give an insight into the structure and shape of the material. The thin, flake-like particles are presented in each sample. The samples showed even structure having extensive surface modification with small porous surface development and craters due to the leaching of an activating agent [46]. It is clearly seen that the polypropylene fibres (Fig. S2a) were completely damaged after the carbonization.

In order to evaluate the textural properties of the carbon-based electrode materials, N_2 adsorption–desorption studies were carried. The values of specific surface areas, total pore volume, micropore volume, and mesopore volume were presented in Table 1.

There are no values characterising the disposable face masks in the Table 1 because the porosity of the mask was so low that it was impossible to obtain the isotherm data or even data points for the BET method. On the basis of the mass of the sample and manual sorptometer can be assumed that surface area of the face mask was below 1 m^2/g. The activation by KOH and carbonization of the face mask boosted porosity fabricating materials suitable for electrode applications.

Table 1
The values of the textural parameters of carbon-based electrode materials.

Carbon-based electrode materials	S_{BET} [m^2/g]	V_{tot} [cm^3/g]	V_{mic} [cm^3/g]
600	460	0.311	0.173
650	685	0.436	0.245
700	752	0.556	0.176
750	969	0.635	0.214
800	746	0.430	0.279

The specific surface area of carbon materials increased with the carbonization temperature from 600 °C to 750 °C, achieved the maximum value of 969 m^2/g and then decreased to 800 °C. These specific surface area values ranged from 460 m^2/g to 969 m^2/g. As a result of the thermal treatment of the disposable face masks, the specific surface area was changed and the total volume of pores and micropores. The total pore volume was calculated assuming the complete filling of pores by N_2 at $p / p_0 = 0.99$, it increased as the carbonization temperature increased to 750 °C and ranged from 0.311 cm^3/g to 0.635 cm^3/g. The most developed porous structure was observed for carbon-based electrode material obtained at the temperature of 750 °C. For the sample 750 S_{BET} and V_{tot} values are also the highest.

The specific surface area was increased with heat treatment because the degree of carbon source oxidation was higher at higher temperatures. In this way the micopores and mesopores pore volume was growing with the temperature up to 750 °C. At 800 °C, oxidation intensity was too high to further develop the micro- and mesopores. The oxidation of the face masks waste at 800 °C was very intensive and mainly macropores were produced which led to a lowering micro- and mesopores volume (see Table 1) and consequently a decrease of specific surface area N_2 adsorption–desorption isotherms at the temperature of −196 °C are presented in Fig. S3.

The isotherms are combinations of I- type characteristics for microporous materials and IV- type characteristics for mesoporous materials defined by the International Union of Pure and Applied Chemistry. For low values of p/p_0 the nitrogen adsorption increased very fast what is typical for microporous materials. That indicated the presence of both micro and mesopores in the material, which can be additionally confirmed based on the pore size distribution. The hysteresis loop is defined as the H3 type, which suggests that they are slit pores indicating the presence of non-uniform, slit-shaped pores. This type is often found with micro-mesoporous carbon [47].

The pore size distribution is presented in Fig. 3. The applied method allowed to calculate pore size distribution to pore diameter 50 nm but the pores with a diameter higher than 14 nm were not observed. All samples exhibited pores smaller than 2 nm. Pores in the range of 2 – 12 nm were also observed. The highest share of mesopores was observed for 700 and 750 samples.

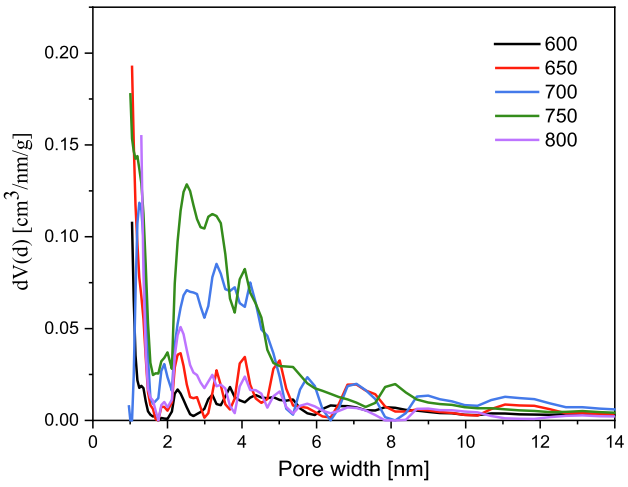

Fig. 3. Carbons pore size distribution determined by DFT method on the basis of N_2 adsorption isotherms.

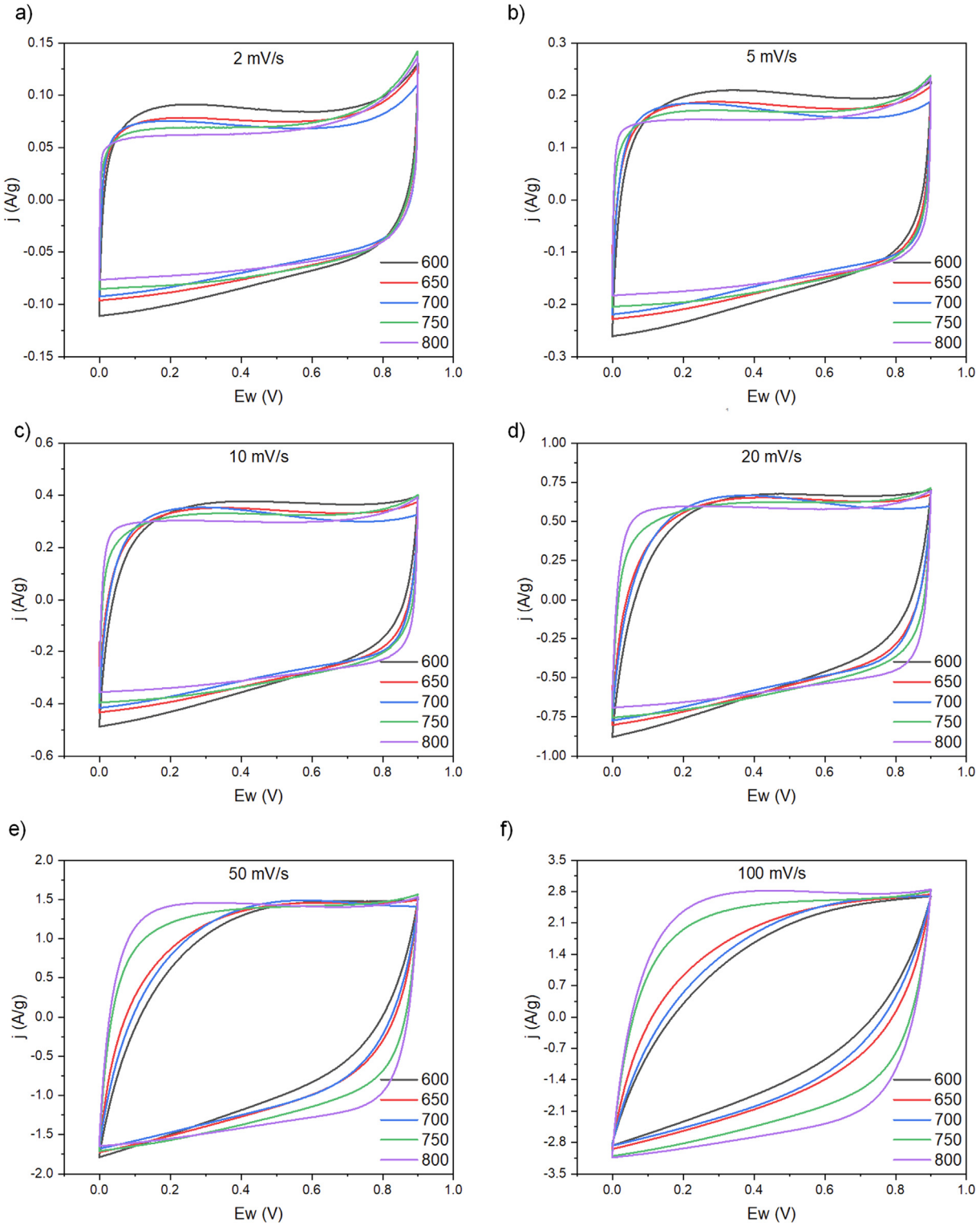

Fig. 4. CV plots of the 2-el cell with 6 M KOH as the electrolyte for all samples at scan rate of (a) 2, (b) 5, (c) 10, (d) 20, (e) 50, and (f) 100 mV/s, respectively.

The results showed that the temperature of the activation process has a strong effect on the texture of carbon derived from disposable face masks. The carbon-based electrode materials obtained by treating KOH and carbonization at N_2 showed high micro-mesopores content, higher surface area and high total pore volume due to intercalation of active K molecules with carbon lattices and carbon matrix than when using other activators [48–50].

Raman spectra of the four studied samples are presented in Fig. S4. All spectra have two peaks, typical for carbon material, around 1350 cm^{-1} (D-band) and 1584 cm^{-1} (G-band). A lower Raman mode (D-band) is associated with disordered carbon such as non-crystalline structures and defective structures. At a higher Raman mode (G-band), the order-layered graphite with sp^2-hybridized carbon atoms vibration is assigned. In all tested

samples, the intensity of the D band is dominant than that of the G band, which indicates the presence of defected carbons in the samples [51,52]. Sample quality is assessed using the ratio of D and G band intensities (I_D/I_G). A lower I_D/I_G value indicates a higher degree of graphitization. The determined values of the I_D/I_G ratio given in Fig. S4 ranged from 1.07 to 1.26 and were similar to the values of other carbon materials [53]. Carbon 650 (I_D/I_G = 1.07) prepared at 650 °C is more structured than the carbon 750 (I_D/I_G = 1.26). XRD analysis of the carbons confirmed the results of Raman spectroscopy. The XRD profiles (not presented here) revealed a predominantly amorphous structure. Moreover, Raman of the commercially available mask was measured (Fig. S5). The mask was divided into 3 layers: outer-, middle- and interlayer and measured individually (see inset of Fig. S5). All obtained spectra were perfectly matched to the polypropylene profile without any shifts. The main peaks are located at 172, 265, 329, 395, 454, 540, 597, 778, 813, 843, 900, 977, 1001, 1044, 1094, 1157, 1219, 1324, 1352, 1465 and peaks at the range 2848–2973 cm^{-1}. In the

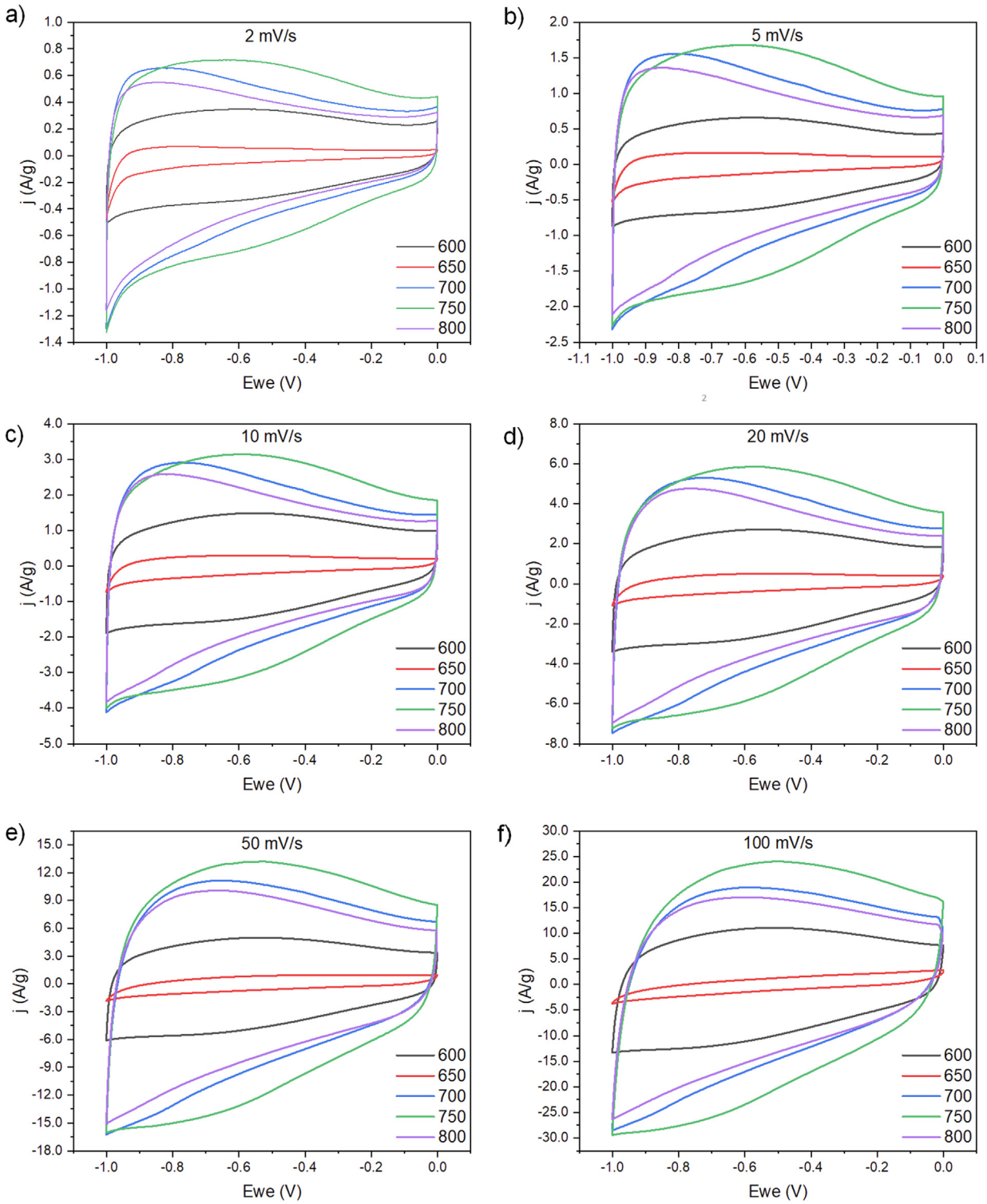

Fig. 5. CV plots of the 3-el cell with 6 M KOH as the electrolyte for all samples at the scan rate of (a) 2, (b) 5, (c) 10, (d) 20, (e) 50, (f) 100 mV/s, respectively.

outer layer plot, 3 new peaks arose at 680, 750 and 1539 cm^{-1}, which can be due to the presence of blue dye in this section [54].

The carbon content and thermal stability in all samples were studied by the Thermogravimetric Analysis (TGA) (Fig. S6). The measurements were conducted with an airflow of 100 cm^3/min air, in the temperature range from 17 to 700 °C and a heating rate of 10 °C/min). The 1st stage corresponds to the first weight loss of 8.7 wt% (in sample 750) to 16.0 wt% (in 700), in the range from room temperature to ~ 58 °C, which was caused by the desorption of humidity. A further plateau presents the 2nd stage. The 3rd stage is a second weight loss with a huge mass decrease in the temperature between 263 and 478 °C (sample 750) and 311 to 523 °C (sample 650), which was due to the combustion of carbon species. The 4th stage is depicted as the final plateau. It refers to the ash content in samples, which was found to be ~ 19.3, 14.3, 12.6, 7.6, and 2.4 wt% for 650, 750, 600, 800, and 700, respectively. The results were used to calculate the carbon content in the samples. Which was found to be the highest (80.5 wt%) sample carbonized at 800 °C and the lowest (69.5 wt%) carbonized at 650 °C. For comparison, the TGA of the commercially available pristine protective mask was also conducted. In the 1st stage, the mask shows the plateau indicating thermal stability up to ~ 150 °C. Further, the material was partially oxidized which is indicated by a slight mass increase of 2.0 wt% between ~ 150 and 220 °C. The intense decrease in mass starts at ~ 220 °C and the complete combustion of material was detected at ~ 470 °C. In the sample made with a pristine mask, there was no residual ash, which is in full agreement with the literature analysis of polypropylene [55].

3.3. Electrochemical results and discussion

3.3.1. Cyclic Voltammetry

The electrochemical properties of the activated carbons were firstly investigated in a two-electrode system composed of 2 identical working electrodes (WE) containing active material and with a separator between them and a 6 M KOH as an electrolyte. Fig. 4 presents the results of the CV technique conducted in the 2-el at different scan rates of 2, 5, 10, 20, 50, and 100 $mV{\cdot}s^{-1}$, in the potential window between 0.0 and + 0.8 V. The CV plots at low scan rates (from 2 to 20 $mV{\cdot}s^{-1}$) show almost rectangular shapes, what is expected for the proper capacitor devices with the subtle faradays edges at the ends of the voltage scan range. The curves do not show any evident redox peaks, indicating the predominant role of classical double-layer capacitive behavior. At the highest scan rate (50 and 100 $mV{\cdot}s^{-1}$) the curves show a flattening effect and begin to create an eye-like shape, which proves a gradual decrease in capacitive properties.

Further, the electrochemical performance of the samples was also investigated in a three-electrode system. Fig. 5 shows the results of the CV technique performed in the 3-el at 2, 5, 10, 20, 50, and 100 $mV{\cdot}s^{-1}$ scan rate, in the potential window between 0.0 and −1.0 V vs MOSE. It is clearly seen that the CV curves have shown slight deviations from the perfect shape. In addition, sharp edges indicate a decrease in capacitive behavior.

3.3.2. Galvanostatic cycling with potential Limitation

The results of specific capacitance (C_s) are presented in Table 2 and Table 3 for 2-el and 3-el systems, respectively. They were calculated according to the equation (1):

$$C_s\left[\frac{F}{g}\right] = \frac{2}{Z} \times \frac{I}{m_a}\frac{dt_{dis}}{dE} = \frac{2}{Z} \times j\frac{dt}{dE} \quad (1)$$

where C_s [$F{\cdot}g^{-1}$] is specific capacitance, m_a [mg] is a total mass of active material, dt_{dis} [s] is a discharge time, I [A] is applied current, dE [V] is the change of potential and Z is a parameter with respect to the type of system (Z = 0.5 for a 2-el, and Z = 1 for a 3-el cell).

The highest specific capacitance at a current density of 0.1 $A{\cdot}g^{-1}$ was achieved by 650, 700 and 750 samples with the values of 132, 139 and 139 in 2-el and 569, 559 and 651F/g in 3-el, respectively. In general, the electric double-layer capacitance (EDLC) increases along with the increase in BET surface area (S_{BET}) of the samples as one of the most important parameters in electrochemical performance. Additionally, the pore size distribution of the active material matching the size of electrolyte ions is also a key characteristic boosting the device's capacitance. In the sample carbonized at 700 °C new pores aroused with the width of ~ 5–6, 7–8, 9, 11 nm, which were not present in the sample carbonized at 750 °C. Those pores are additional channels for electrolyte ions diffusion. Considering its pore size and S_{BET} of 750 samples (969 m^2/g), its capacitance is the most boosted.

Charging and discharging plots measured in a 2-el are presented in Fig. 6. This technique was conducted in imposed current density: 0.1, 0.6, 1.0, 6.5, and 13.0 $A{\cdot}g^{-1}$, respectively, in the potential window between 0.0 and + 0.8 V. The specific capacitance of the material was obtained from the galvanostatic cycling with potential limitations (GCPL) test at a variable constant current and then calculated with respect to equation (1) below. All results were presented in a plot showing the dependence of capacitance vs current density (Fig. 6f). In the low current density (from 0.1 to 6.5 $A{\cdot}g^{-1}$), the charge–discharge curves have shown an almost symmetrical, triangle shape, expected for capacitive-like behavior. The triangular form confirmed that none of the redox reactions proceeded during the work of the devices. An increase in the current density, analogically to the scan rates in the case of CV measurement, leads to a decrease in the ion migration to the

Table 2
The specific capacitance in the 2-el for all obtained samples.

Electrochemical parameters in the 2-el (0.1 A/g)					
Sample	600	650	700	750	800
dt_{dis} [s]	184.34	202.61	213.12	213.35	204.78
Cs [F/g]	119.8	131.7	138.5	138.7	133.1

Table 3
The specific capacitance in the 3-el for all obtained samples.

Electrochemical parameters in the 3-el (0.1 A/g)					
Sample	600	650	700	750	800
dt_{dis} [s]	1520	2362	2320	2702	1875
Cs [F/g]	366.4	569.2	559.0	651.1	451.8

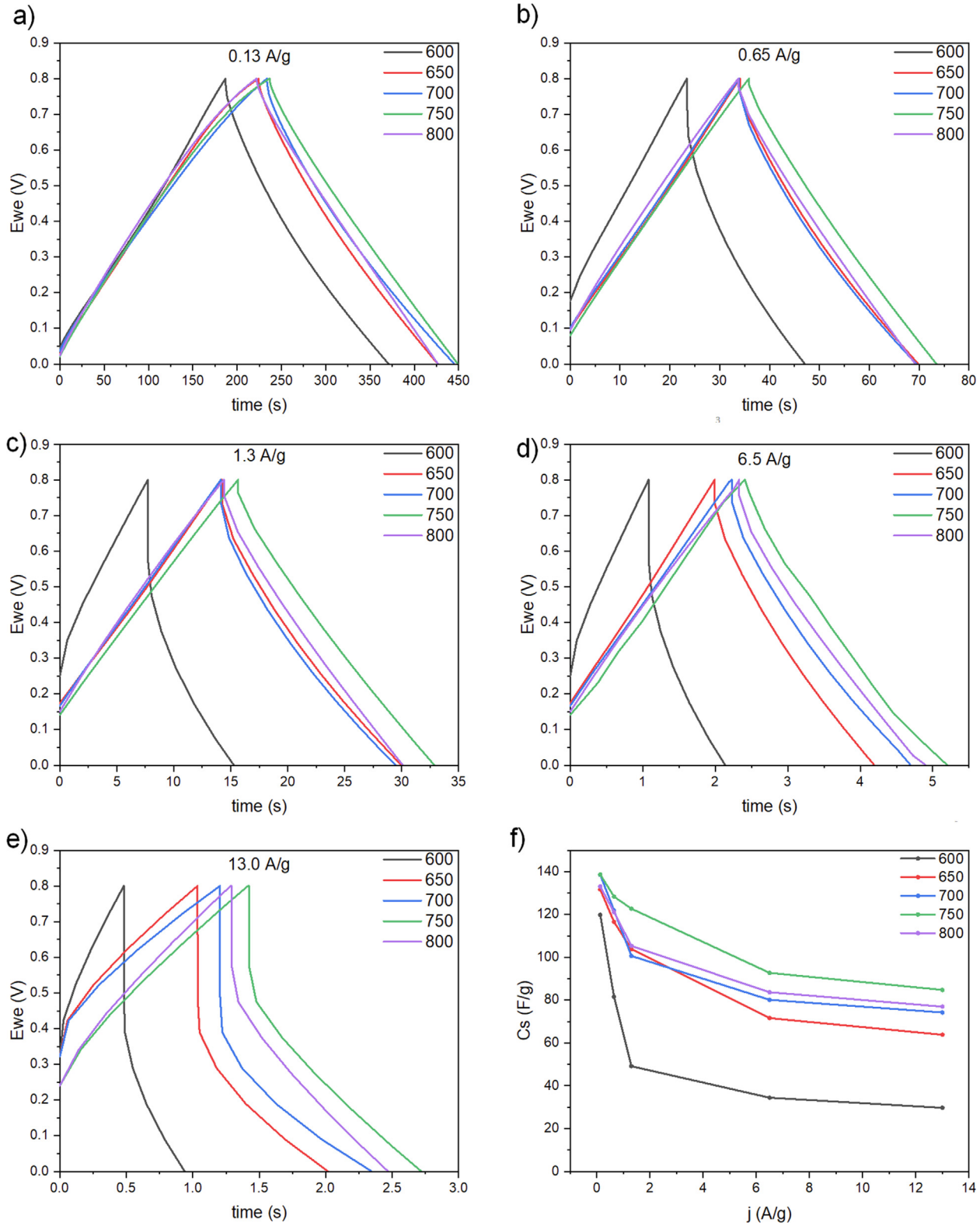

Fig. 6. Charging-discharging curves for the 2-el cell conducted at (a) 0.1, (b) 0.6, (c) 1.0, (d) 6.5, and (e) 13.0 A·g^{-1} current densities, (f) specific capacitance vs different current densities for all samples.

diffusion layer, which in consequence decreases the rate of the faradaic process.

The same plots measured in a 3-el are presented in Fig. 7. In this case, the measurements were carried out in imposed current density: 0.1 A·g^{-1}, in the potential window between 0.0 and 1.0 V vs MOSE. The shape of the GCPL plot is almost ideally triangular, but the sample carbonized at 650 °C shows the highest IR drop, corresponding to the interface resistance.

The values of the C_s of all the samples measured in 3-el measurements are higher than that obtained in a 2-el cell. Therefore, the remaining electrochemical results will be presented in details for 3-el.

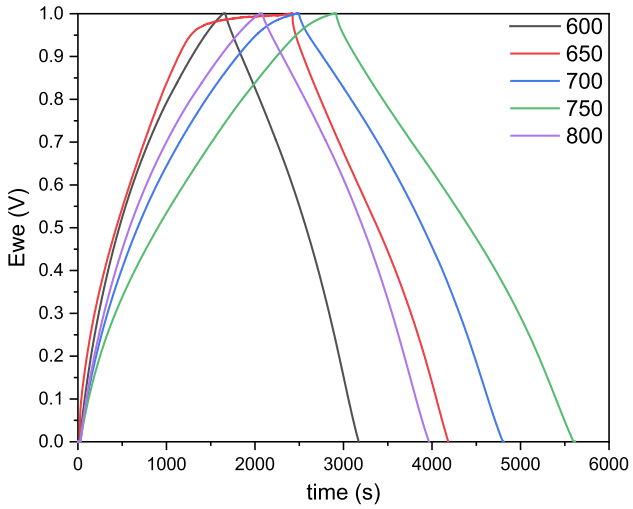

Fig. 7. Charging-discharging curves for the 3-el cell conducted at 0.1 A·g^{-1}.

To obtain information about charge transfer and to study double-layer structure, electrochemical impedance spectroscopy in potentiostatic mode (PEIS) was conducted in the frequency range: 200 kHz and 10 mHz, with 10 mV of alternating current amplitude (AC signal). Fig. 8 a and b show the results, which were fitted with the equivalent circuit of R1 + Q2/R2. Table 4 presents calculated parameters based on these measurements. This equivalent circuit consists of an electrolyte resistance R1 [Ω], a charge transfer resistance R2 [Ω] and a constant phase element (CPE) Q [F*s$^{(a-1)}$]. The first point on a real axis (at the highest frequency (HF) of measurement), is the sum of the resistance of the electrolyte and all the switches connected in series and is presented as R1. The diameter of this semicircle is the value of the charge transfer resistance (R2). The Nyquist diagram of Q-element (CPE) corresponds to a straight line in positive imaginary part (-Im (Z) > 0) with angle -απ/2 with the 0X axis. The faradic impedance of the CPE decreases with increasing frequency. In this situation, α is the dispersion coefficient, which is a unitless number with the value 0 < α ≤ 1, where α = 1 corresponds to ideal capacitive behaviour. The schematic interpretation of the (PEIS) diagram is present in Fig. 8 c. Equivalent series resistance (ESR), or so-called internal resistance, is the value that determines the loss of energy in a simple electronic circuit consisting of a resistor and an ideal capacitor. The presentation of ESR at the Nyquist plot is a sum of R1 and R2 resistances. The rest of the Nyquist plot corresponds to the lower frequency (LF) and goes into a straight line, which corresponds to the capacitive element. Extrapolating the linear range to the 0X axis allows the calculation of the value of the equivalent distributed resistance (EDR) according to transmission line theory to check the behaviour of a supercapacitor when a pulsed current flows through it [56,57].

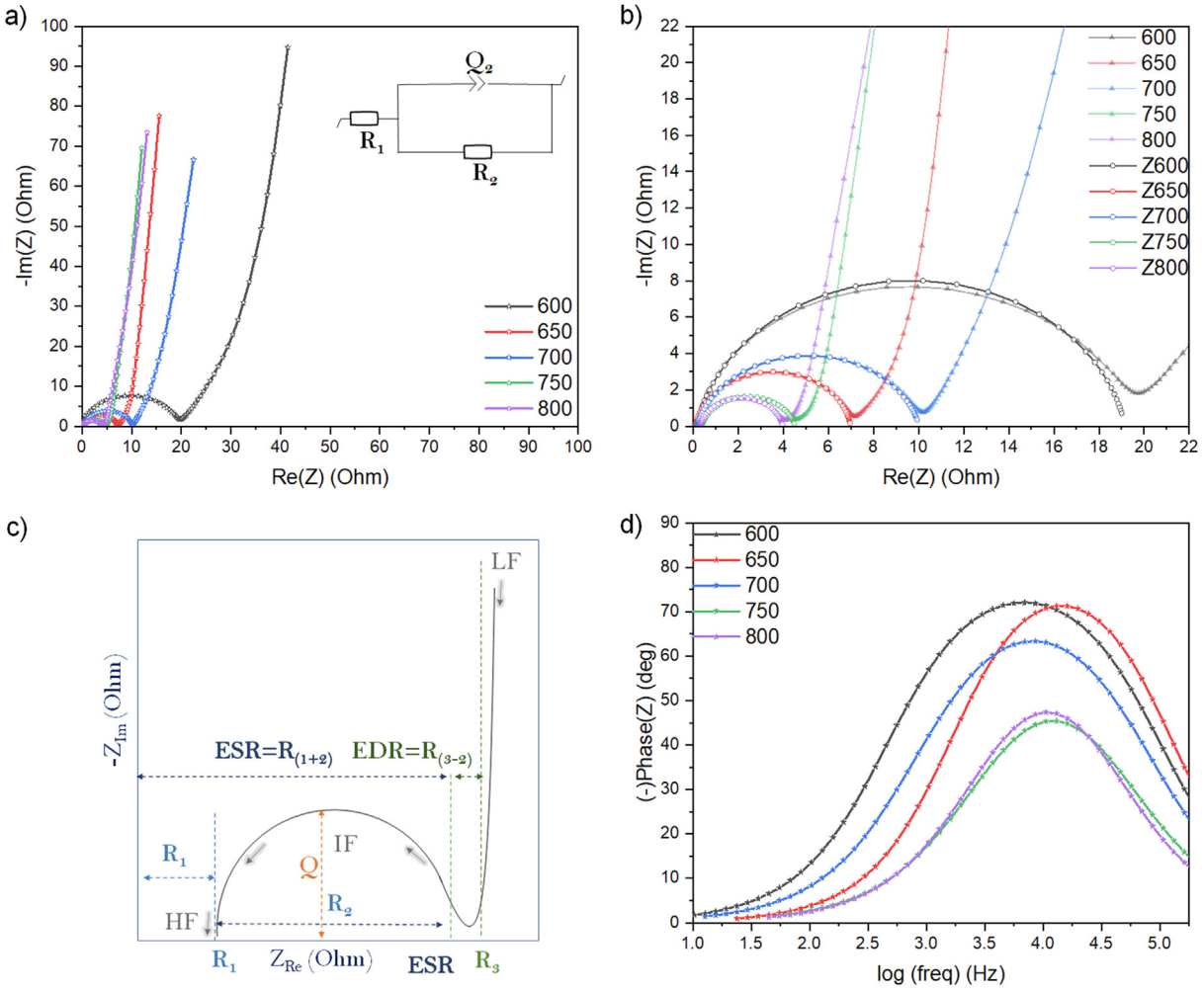

Fig. 8. Results of the PEIS measurement: (a) Nyquist plot for the all obtained samples, with the insert of the applied equivalent circuit electrical scheme (R1 + Q2/R2), (b) magnification of the EIS Nyquist in the HF region with Z-fit applied (Z-fit labe), c) schematic illustration of EIS interpretation and d) Bode plot (phase angle-frequency).

Table 4
Analysis of the electrochemical parameters obtained via PEIS measurements.

Analysis of the EIS Nyquist in the 2-el					
Sample	600	650	700	750	800
R1 [Ω]	0.14	0.09	0.16	0.30	0.32
Q2 [$Fs^{\alpha-1}$]	40.27 x10^{-6}	27.76 x10^{-6}	68.45 x10^{-6}	78.72 x10^{-6}	54.10x10^{-6}
α	0.909	0.955	0.871	0.851	0.889
R2 [Ω]	17.65	5.61	8.26	2.91	2.97
ESR [Ω]	17.79	5.70	8.42	3.21	3.29
EDR [Ω]	21.21	7.97	11.99	7.31	8.83
x_0	20.42	7.67	10.59	4.93	4.36
x_{max}	41.63	15.64	22.58	12.24	13.19
Slope [Ω/ Ω]	3.41	10.42	5.05	10.79	8.75
arctang(slope)	73.65	84.52	78.79	84.71	83.48

Table 5
Specific energy and power of materials.

Analysis of the energy density and power density for the 1.2 mA g^{-1}					
Sample	600	650	700	750	800
E [$\frac{Wh}{kg}$]	19.17	21.07	22.17	22.19	21.30
P [$\frac{W}{kg}$]	0.97	3.04	2.06	5.40	5.27

The Nyquist PEIS plots for all tested wasted mask-derived materials have a similar shape, which starts with semicircles. The overall geometry of plots is suitable for a material with capacitive characteristics (Fig. 8 a, b). Moreover, the plots start at almost the same value of real resistance (R1), with the maximum difference of 0.23 Ω (Table 4), indicating almost identical parameters for carrying out the process, i.e. electrolyte and current connector resistance. The main difference is the size of the half-circle, which is attributed to a change in the value of R2. The lowest R2 has the samples carbonized at 750, and 800 °C with the values of 2.91, and 2.97 Ω, respectively, indicating the most favourable capacitive behaviour. These results are in agreement with ESR and EDR values, in which samples carbonized at 750 and 800 °C have the lowest values of 3.2, 3.29 Ω (ESR) and 7.31, 8.83 Ω (EDR), correspondingly. These PEIS analyses confirm low internal resistance of the system, which indicates the outstanding performance of the mask-derived carbon as supercapacitor devices.

Moreover, PEIS results are also presented as a Bode plot (Fig. 8 d). In the ideal capacitors, the maximum phase angle occurs at 90°. The phase angle of 72.2, and 71.5° (for 600, and 650 samples, respectively) are the closest value to the perfect 90° angle. Next samples indicate the following angles: 63.3, 47.6, and 45.6° for 700, 800, and 750, respectively. Therefore, ion charge transfer through the electrode/electrolyte interface is the most efficient in the carbon activated at 600 °C.

3.3.3. Ragone plot

The Ragone plot is used to compare the working range of the energy density and the specific power for the various energy storage devices. These parameters were calculated using the following equations, (2, 3) and are presented in Table 5.

$$E_s\left[\frac{Wh}{g}\right] = \frac{I \times dU \times dt}{m_a} \tag{2}$$

$$P_s\left[\frac{W}{g}\right] = \frac{U^2}{m_a \times 4 \times ESR} \tag{3}$$

where Es is the specific energy and Ps is the specific power, other parameters are corresponding to the discharge step.

The graphic relationships between specific energy vs specific power are shown as a Ragone plot in Fig. 9.

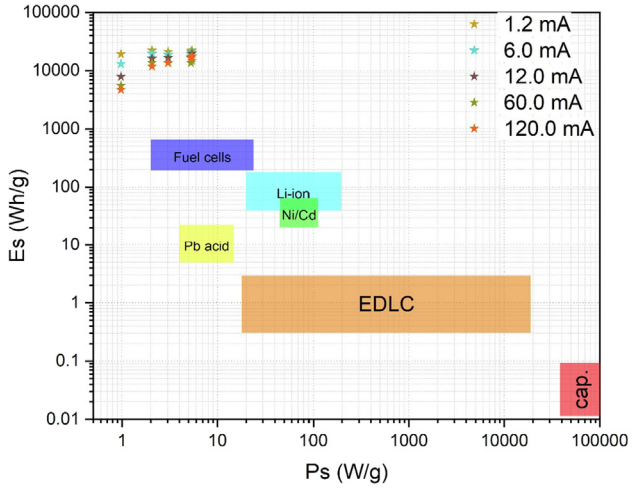

Fig. 9. Ragone plot showing specific energy vs specific power plot for all synthesized samples (stars) in comparison to common electrical energy storage devices.

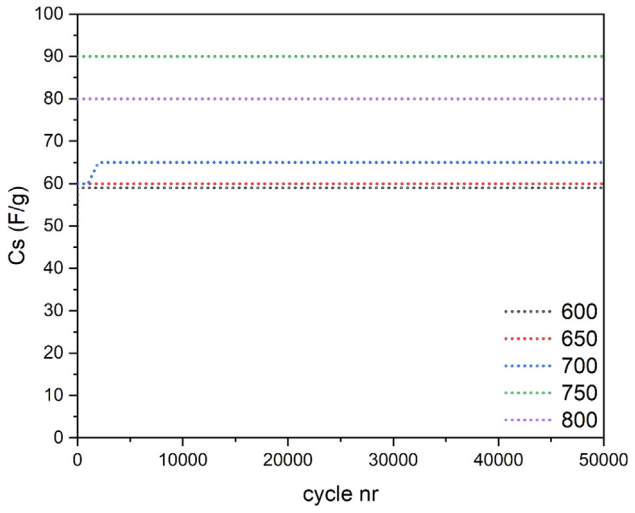

Fig. 10. Stability of the specific capacitance during cycling test (for 50′000 cycles) conducted at the current density of 2 A·g^{-1}.

Table 6
Comparison of specific capacitance of different recycled carbon-based supercapacitors.

Material	Source of carbon	j [A/g]	Cs [F/g]	Ref.
O—N—S co-doped carbon	lotus leaf stem	0.5	425	[36]
nitrogen- and sulphur-doped carbon	foxtail grasses seeds	0.5	358	[37]
graphene-like porous carbon networks	orange-peel	0.5	425	[38]
Porous carbon	Cellulose	0.5	162	[40]
Porous carbon	Lignin	1.0	325	[39]
Porous carbon	bottle (PET)	1.0	413	[41]
Porous carbon	Polystyrene foam (PS)	1.0	327	[42]
Porous carbon	Protective mask (PP)	1.0	329	[43]
Porous carbon	**protective mask (PP)**	**0.1**	**651**	**Our work**

3.3.4. Stability test

Furthermore, for a complete description of the electrode material, the stability tests have been conducted. The material used in supercapacitors should exhibit as high-power capacity as possible and high durability during long-lasting operation. In other words, the goal is to have the lowest possible difference in capacity.

To test the performance of electrode material the charge–discharge test was conducted under the constant current density of 2 $A{\cdot}g^{-1}$ for 50′000 cycles. The results are presented in Fig. 10. The specific capacitance retention of all materials is excellent. Almost constant values through as many as 50′000 repetitions indicate that there is reversible charging and discharging at the interface between the electrode and the electrolyte.

Furthermore, in order to verify the electrochemical potential of our materials used in supercapacitors the comparison to the respective reports in state-of-the-art is presented in Table 6. Our outstanding performance can be due to our materials' optimal textural characteristics, allowing the best working condition in supercapacitors (SC devices).

4. Conclusions

Carbon-based electrode materials were prepared from potentially contaminated disposable face masks – waste which is currently produced in enormous amounts because of the ongoing coronavirus pandemic – COVID-19. The material synthesized showed an enhanced specific surface area and the presence of micro- and mesopores. The macropores' volumes were much larger than the micropores. It was shown that the temperature of the carbonization at the constant ratio of KOH reagent to carbon source greatly affected the textural properties of the materials.

The influence of the temperature during the carbonization process in the range between 600 and 800 °C on electrochemical performance as electrode materials in SC has been revealed. It is worth mentioning that the mass loading during the test was at around 10 mg per device, which is a great advantage, as it is known, that this parameter is one of the most important obstacles during EDLC design. Moreover, every sample has exhibited great performance during the stability test, keeping stable charge–discharge capability over as many as 50′000 cycles, which is one of the requirements for materials used as electrodes in the supercapacitors devices.

In conclusion, the positive results from this present study have established the feasibility of carbon-based electrode materials production from potentially contaminated disposable face masks combined with absolutely destroying all microorganisms, including coronaviruses. Activated carbon prepared from contaminated disposable face masks was characterized by a large surface area, high total pore volume, and good charge-holding capacity. Therefore, these properties make it suitable material for the carbon electrode of supercapacitors. The optimal electrode material has resulted in the performance of a supercapacitor (SC) device with excellent parameters such as specific capacitance attaining 651.1F/g at 0.1 Ag^{-1}, specific energy of 22.19 Wh kg^{-1}, and power density of 5.40 Wkg^{-1} at current density = 1.2 mA g^{-1} in a voltage window of 0–0.8 V. Furthermore, the outstanding capacitance retention of 98 % was obtained after a test cycle involving 50′000 cycles.

CRediT authorship contribution statement

Joanna Sreńscek-Nazzal: Conceptualization, Methodology, Formal analysis, Investigation, Writing – original draft, Writing – review & editing, Visualization. **Jarosław Serafin:** Conceptualization, Methodology, Validation, Formal analysis, Investigation, Data curation, Writing – original draft, Writing – review & editing, Visualization. **Adrianna Kamińska:** Methodology, Formal analysis, Investigation, Data curation, Writing – original draft, Writing – review & editing, Visualization. **Anna Dymerska:** Methodology, Formal analysis, Investigation, Data curation, Writing – original draft, Writing – review & editing. **Ewa Mijowska:** Conceptualization, Validation, Data curation, Writing – original draft, Writing – review & editing, Supervision. **Beata Michalkiewicz:** Conceptualization, Validation, Data curation, Writing – original draft, Writing – review & editing, Supervision.

Declaration of Competing Interest

The authors declare that they have no known competing financial interests or personal relationships that could have appeared to influence the work reported in this paper.

Acknowledgements

Jarosław Serafin is grateful to Spanish Ministry of Research and Innovation project no: PID2020-116031RBI00/AEI/10.13039/501100011033/FEDER.

Appendix A. Supplementary material

Supplementary data to this article can be found online at https://doi.org/10.1016/j.jcis.2022.07.098.

References

[1] M. Sendra, P. Pereiro, M.P. Yeste, B. Novoa, A. Figueras, Surgical face masks as a source of emergent pollutants in aquatic systems: Analysis of their degradation product effects in Danio rerio through RNA-Seq, J. Hazard. Mater. 428 (2022), https://doi.org/10.1016/j.jhazmat.2021.128186 128186.
[2] M. Kalina, F. Ali, E. Tilley, "Everything continued as normal": What happened to Africa's wave of Covid-19 waste?, Waste Manag 120 (2021) 277–279, https://doi.org/10.1016/j.wasman.2020.11.051.
[3] J.R. Jambeck, R. Geyer, C. Wilcox, T.R. Siegler, M. Perryman, A. Andrady, R. Narayan, K.L. Law, Plastic waste inputs from land into the ocean, Science 347 (No.6223) (2015) 768–771, https://doi.org/10.1126/science.1260352.
[4] S.L. Wu, J.H. Kuo, M.Y. Wey, Thermal degradation of waste plastics in a two-stage pyrolysis-catalysis reactor over core-shell type catalyst, J. Anal. Appl. Pyrolysis. 142 (2019), https://doi.org/10.1016/j.jaap.2019.104641 104641.

[5] L. Makarichi, W. Jutidamrongphan, K. anan Techato,, The evolution of waste-to-energy incineration: A review, Renew, Sustain. Energy Rev. 91 (2018) 812–821, https://doi.org/10.1016/j.rser.2018.04.088.
[6] E.S. Windfeld, M.-S.-L. Brooks, Medical waste management – A review, J. Environ. Manage. 163 (2015) 98–108, https://doi.org/10.1016/j.jenvman.2015.08.013.
[7] R. Yu, X. Wen, J. Liu, Y. Wang, X. Chen, K. Wenelska, E. Mijowska, T. Tang, A green and high-yield route to recycle waste masks into CNTs/Ni hybrids via catalytic carbonization and their application for superior microwave absorption, Appl. Catal. B Environ. 298 (2021), https://doi.org/10.1016/j.apcatb.2021.120544 120544.
[8] S. Jung, S. Lee, X. Dou, E.E. Kwon, Valorization of disposable COVID-19 mask through the thermo-chemical process, Chem. Eng. J. 405 (2021), https://doi.org/10.1016/j.cej.2020.126658 126658.
[9] G. Xu, H. Jiang, M. Stapelberg, J. Zhou, M. Liu, Q.J. Li, Y. Cao, R. Gao, M. Cai, J. Qiao, M.S. Galanek, W. Fan, W. Xue, B. Marelli, M. Zhu, J. Li, Self-perpetuating carbon foam microwave plasma conversion of hydrocarbon wastes into useful fuels and chemicals, Environ. Sci. Technol. 55 (2021) 6239–6247, https://doi.org/10.1021/acs.est.0c06977.
[10] X. Liu, C. Ma, Y. Wen, X. Chen, X. Zhao, T. Tang, R. Holze, E. Mijowska, Highly efficient conversion of waste plastic into thin carbon nanosheets for superior capacitive energy storage, Carbon N. Y. 171 (2021) 819–828, https://doi.org/10.1016/j.carbon.2020.09.057.
[11] Z. Jiang, R. Song, W. Bi, J. Lu, T. Tang, Polypropylene as a carbon source for the synthesis of multi-walled carbon nanotubes via catalytic combustion, Carbon N. Y. 45 (2007) 449–458, https://doi.org/10.1016/j.carbon.2006.08.012.
[12] M. Notarianni, J. Liu, K. Vernon, N. Motta, Synthesis and applications of carbon nanomaterials for energy generation and storage, Beilstein J. Nanotechnol. 7 (2016) 149–196, https://doi.org/10.3762/bjnano.7.17.
[13] P. Kalyani, A. Anitha, Biomass carbon & its prospects in electrochemical energy systems, Int. J. Hydrogen Energy. 38 (2013) 4034–4045, https://doi.org/10.1016/j.ijhydene.2013.01.048.
[14] R. Kumar, R.K. Singh, D.P. Singh, Natural and waste hydrocarbon precursors for the synthesis of carbon based nanomaterials: Graphene and CNTs, Renew. Sustain. Energy Rev. 58 (2016) 976–1006, https://doi.org/10.1016/j.rser.2015.12.120.
[15] S. Nasir, M. Hussein, Z. Zainal, N. Yusof, S. Mohd Zobir, Electrochemical Energy Storage Potentials of Waste Biomass: Oil palm leaf- and palm kernel shell-derived activated carbons, Energies. 11 (2018) 3410, https://doi.org/10.3390/en11123410.
[16] J. Deng, M. Li, Y. Wang, Biomass-derived carbon: Synthesis and applications in energy storage and conversion, Green Chem. 18 (2016) 4824–4854, https://doi.org/10.1039/c6gc01172a.
[17] L. Dai, D.W. Chang, J.-B. Baek, W. Lu, Carbon nanomaterials for advanced energy conversion and storage, Small. 8 (2012) 1130–1166, https://doi.org/10.1002/smll.201101594.
[18] M. Inagaki, H. Konno, O. Tanaike, Carbon materials for electrochemical capacitors, J. Power Sources. 195 (2010) 7880–7903, https://doi.org/10.1016/j.jpowsour.2010.06.036.
[19] K. Mensah-Darkwa, C. Zequine, P.K. Kahol, R.K. Gupta, Supercapacitor energy storage device using biowastes: A sustainable approach to green energy, Sustain. 11 (2019) 414, https://doi.org/10.3390/su11020414.
[20] W. Kukulka, K. Cendrowski, B. Michalkiewicz, E. Mijowska, MOF-5 derived carbon as material for CO2 absorption, RSC Adv. 9 (2019) 18527–18537, https://doi.org/10.1039/C9RA01786K.
[21] S. Maji, R.G. Shrestha, J. Lee, S.A. Han, J.P. Hill, J.H. Kim, K. Ariga, L.K. Shrestha, Macaroni Fullerene Crystals-Derived Mesoporous Carbon Tubes as a High Rate Performance Supercapacitor Electrode Material, BCSJ 94 (5) (2021) 1502–1509.
[22] H. Demiral, I. Demiral, B. Karabacakoğlu, F. Tümsek, Production of activated carbon from olive bagasse by physical activation, Chem. Eng. Res. Des. 89 (2011) 206–213, https://doi.org/10.1016/j.cherd.2010.05.005.
[23] K.-C. Lee, M.S.W. Lim, Z.-Y. Hong, S. Chong, T.J. Tiong, G.-T. Pan, C.-M. Huang, Coconut shell-derived activated carbon for high-performance solid-state supercapacitors, Energies. 14 (2021) 4546, https://doi.org/10.3390/en14154546.
[24] X. Jiang, G. Shi, G. Wang, P. Mishra, C. Liu, Y. Dong, P. Zhang, H. Tian, Y. Liu, Z. Wang, Q. Zhang, H. Zhang, A hydrothermal carbonization process for the preparation of activated carbons from hemp straw: an efficient electrode material for supercapacitor application, Ionics (Kiel). 25 (2019) 3299–3307, https://doi.org/10.1007/s11581-019-02850-8.
[25] E. Taer, R. Taslim, A.W. Putri, A. Apriwandi, A. Agustino, Activated carbon electrode made from coconut husk waste for supercapacitor application, Int. J. Electrochem. Sci. 13 (2018) 12072–12084. https://doi.org/10.20964/2018.12.19.
[26] K. Kuratani, K. Okuno, T. Iwaki, M. Kato, N. Takeichi, T. Miyuki, T. Awazu, M. Majima, T. Sakai, Converting rice husk activated carbon into active material for capacitor using three-dimensional porous current collector, J. Power Sources. 196 (2011) 10788–10790, https://doi.org/10.1016/j.jpowsour.2011.09.001.
[27] J. Serafin, M. Baca, M. Biegun, E. Mijowska, R.J. Kaleńczuk, J. Sreńscek-Nazzal, B. Michalkiewicz, Direct conversion of biomass to nanoporous activated biocarbons for high CO2 adsorption and supercapacitor applications, Appl. Surf. Sci. 497 (2019) 143722.
[28] W. Sangchoom, D.A. Walsh, R. Mokaya, Valorization of lignin waste: High electrochemical capacitance of lignin-derived carbons in aqueous and ionic liquid electrolytes, J. Mater. Chem. A. 6 (2018) 18701–18711, https://doi.org/10.1039/c8ta07632d.
[29] L.-H. Zheng, M.-H. Chen, S.-X. Liang, Q.-F. Lü, Oxygen-rich hierarchical porous carbon derived from biomass waste-kapok flower for supercapacitor electrode, Diam. Relat. Mater. 113 (2021), https://doi.org/10.1016/j.diamond.2021.108267 108267.
[30] J. Serafin, K. Kiełbasa, B. Michalkiewicz, The new tailored nanoporous carbons from the common polypody (Polypodium vulgare): The role of textural properties for enhanced CO2 adsorption, Chem. Eng. J. 429 (2022), https://doi.org/10.1016/j.cej.2021.131751 131751.
[31] M. Kwiatkowski, J. Serafin, A.M. Booth, B. Michalkiewicz, Computer analysis of the effect of activation temperature on the microporous structure development of activated carbon derived from common polypody, Materials (Basel). 14 (2021) 2951, https://doi.org/10.3390/ma14112951.
[32] J. Serafin, Utilization of spent dregs for the production of activated carbon for CO2 adsorption, Polish, J Chem. Technol. 19 (2017) 44–50, https://doi.org/10.1515/pjct-2017-0026.
[33] J. Serafin, M. Ouzzine, O.F. Cruz Junior, J. Sreńscek-Nazzal, Preparation of low-cost activated carbons from amazonian nutshells for CO2 storage, Biomass Bioenergy 144 (2021), https://doi.org/10.1016/j.biombioe.2020.105925 105925.
[34] M. Ouzzine, J. Serafin, J. Sreńscek-Nazzal, Single step preparation of activated biocarbons derived from pomegranate peels and their CO2 adsorption performance, J. Anal. Appl. Pyrolysis. 160 (2021), https://doi.org/10.1016/j.jaap.2021.105338 105338.
[35] L. He, Y. Sun, C. Wang, H. Guo, Y. Guo, C. Li, Y. Zhou, High performance sulphur-doped pitch-based carbon materials as anode materials for sodium-ion batteries, New Carbon Mater. 35 (2020) 420–427, https://doi.org/10.1016/S1872-5805(20)60499-1.
[36] H. Liu, W. Chen, R. Zhang, Y. Ren, Naturally O-N-S Co-doped carbon with multiscale pore architecture derived from lotus leaf stem for high-performance supercapacitors, Bull. Chem. Soc. Jpn. 94 (6) (2021) 1705–1714, https://doi.org/10.1246/bcsj.20210027.
[37] X. Liang, R. Liu, X. Wu, Biomass waste derived functionalized hierarchical porous carbon with high gravimetric and volumetric capacitances for supercapacitors, Microporous Mesoporous Mater. 310 (2021), https://doi.org/10.1016/j.micromeso.2020.110659 110659.
[38] C. Karaman, O. Karaman, N. Atar, M.L. Yola, Sustainable electrode material for high-energy supercapacitor: biomass-derived graphene-like porous carbon with three-dimensional hierarchically ordered ion highways, Phys. Chem. Chem. Phys. 23 (22) (2021) 12807–12821, https://doi.org/10.1039/D1CP01726H.
[39] W. Chen, M. Luo, K. Yang, X. Zhou, Microwave-assisted KOH activation from lignin into hierarchically porous carbon with super high specific surface area by utilizing the dual roles of inorganic salts: Microwave absorber and porogen, Microporous Mesoporous Mater. 300 (2020), https://doi.org/10.1016/j.micromeso.2020.110178 110178.
[40] D.I. Abouelamaiem, G. He, I. Parkin, T.P. Neville, A.B. Jorge, S. Ji, R. Wang, M.M. Titirici, P.R. Shearing, D.J.L. Brett, Synergistic relationship between the three-dimensional nanostructure and electrochemical performance in biocarbon supercapacitor electrode materials, Sustain, Energy Fuels. 2 (2018) 772–785, https://doi.org/10.1039/c7se00519a.
[41] X. Liu, Y. Wen, X. Chen, T. Tang, E. Mijowska, Co-etching effect to convert waste polyethylene terephthalate into hierarchical porous carbon toward excellent capacitive energy storage, Sci. Total Environ. 723 (2020), https://doi.org/10.1016/j.scitotenv.2020.138055 138055.
[42] N. Deka, J. Barman, S. Kasthuri, V. Nutalapati, G.K. Dutta, Transforming waste polystyrene foam into N-doped porous carbon for capacitive energy storage and deionization applications, Appl. Surf. Sci. 511 (2020), https://doi.org/10.1016/j.apsusc.2020.145576 145576.
[43] X. Hu, Z. Lin, Transforming waste polypropylene face masks into S-doped porous carbon as the cathode electrode for supercapacitors, Ionics (Kiel). 27 (2021) 2169–2179, https://doi.org/10.1007/s11581-021-03949-7.
[44] F.C. Chiu, P.H. Chu, Characterization of solution-mixed polypropylene/clay nanocomposites without compatibilizers, J. Polym. Res. 13 (2006) 73–78, https://doi.org/10.1007/s10965-005-9009-7.
[45] F.J. Lanyi, Modification of interfacial properties of polypropylene fibers using hydrophilic melt additives – interactions with crystallization erlangen, FAU University Press, 2020.
[46] K. Chomiak, S. Gryglewicz, K. Kierzek, J. Machnikowski, Optimizing the properties of granular walnut-shell based KOH activated carbons for carbon dioxide adsorption, J. CO2 Util. 21 (2017) 436–443, https://doi.org/10.1016/j.jcou.2017.07.026.
[47] M. Thommes, K. Kaneko, A.V. Neimark, J.P. Olivier, F. Rodriguez-Reinoso, J. Rouquerol, K.S.W. Sing, Physisorption of gases, with special reference to the evaluation of surface area and pore size distribution (IUPAC Technical Report), Pure Appl. Chem. 87 (2015) 1051–1069, https://doi.org/10.1515/pac-2014-1117.
[48] S. Timur, I.C. Kantarli, S. Onenc, J. Yanik, Characterization and application of activated carbon produced from oak cups pulp, J. Anal. Appl. Pyrolysis. 89 (2010) 129–136, https://doi.org/10.1016/j.jaap.2010.07.002.
[49] A. Heidari, H. Younesi, A. Rashidi, A. Ghoreyshi, Adsorptive removal of CO2 on highly microporous activated carbons prepared from Eucalyptus camaldulensis wood: Effect of chemical activation, J. Taiwan Inst. Chem. Eng. 45 (2014) 579–588, https://doi.org/10.1016/j.jtice.2013.06.007.

[50] J. Chen, L. Zhang, G. Yang, Q. Wang, R. Li, L.A. Lucia, Preparation and characterization of activated carbon from hydrochar by phosphoric acid activation and its adsorption performance in prehydrolysis liquor, BioResources. 12 (2017). https://doi.org/10.15376/biores.12.3.5928-5941.
[51] N.A. Rahma, A. Kurniasari, Y.D. Setyo Pambudi, H.M. Bintang, A. Zulfia, C. Hudaya, Characteristics of corncob-originated activated carbon using two different chemical agent, IOP Conf, Ser. Mater. Sci. Eng. 622 (1) (2019) 012030.
[52] K.K. Kishibayev, J. Serafin, R.R. Tokpayev, T.N. Khavaza, A.A. Atchabarova, D.A. Abduakhytova, Z.T. Ibraimov, J. Sreńscek-Nazzal, Physical and chemical properties of activated carbon synthesized from plant wastes and shungite for CO2 capture, J. Environ. Chem. Eng. 9 (6) (2021) 106798.
[53] S. Wang, H. Cheng, D. Jiang, F. Huang, S. Su, H. Bai, Raman spectroscopy of coal component of Late Permian coals from Southern China, Spectrochim. Acta - Part A Mol. Biomol. Spectrosc. 132 (2014) 767–770, https://doi.org/10.1016/j.saa.2014.06.003.
[54] C. E. B. Dhafer, M. Dhahri, A. Mezni, A., L. S. Smiri, Surface-enhanced Raman scattering study of PP/Ag nanocomposite developed to prevent postsurgery infection. J. of Raman Spectro. 49,9 (2018) 1445-1451. https://doi.org/10.1002/jrs.5412.
[55] G. Zhang, C. Nam, T.M. Chung, L. Petersson, H. Hillborg, Polypropylene copolymer containing cross-linkable antioxidant moieties with long-term stability under elevated temperature conditions, Macromolecules 50 (18) (2017) 7041–7051, https://doi.org/10.1021/acs.macromol.7b01235.
[56] K. Maslana, K. Wenelska, M. Biegun, E. Mijowska, High catalytic performance of tungsten disulphide rodes in oxygen evolution reactions in alkaline solutions, Appl. Catal. B: Environ. 266 (2020), https://doi.org/10.1016/j.apcatb.2019.118575 118575.
[57] B. Bera, T. Kar, A. Chakraborty, M. Neergat, Influence of nitrogen-doping in carbon on equivalent distributed resistance and capacitance–Implications to electrocatalysis of oxygen reduction reaction, J. Electroanal. Chem. 805 (2017) 184–192, https://doi.org/10.1016/j.jelechem.2017.10.025.